Proceedings of the 17th Hypervelocity Impact Symposium
HVIS2024
September 9-13, 2024, Tsukuba, Japan

HVIS2024-009

GENERAL BALLISTIC-LIMIT EQUATIONS FOR WHIPPLE SHIELDS AGAINST LOW- AND HIGH-DENSITY METEOROID SURROGATES

Joshua E. Miller[1,2]*, Bruce (Alan) Davis[2], Kevin D. Deighton[2]

[1] University of Texas at El Paso, El Paso, TX, USA
[2] Jacobs-JETSII, NASA Johnson Space Center, Houston, TX, USA

ABSTRACT

Long-term reliability of habitable volumes requires knowing the onset of a perforation of a hull for crewed vehicles. Previous studies and models have been developed from ground-test data and rely on empirical extrapolations to higher speeds of orbital debris. These extrapolations are to less than twice the speed of ground-test data; therefore, these empirical extrapolations are assumed to be reasonable for many of the current operating vehicles in the orbital debris environment. This assumption may not hold up well for meteoroid impacts as they are expected to occur at impact speeds of 20 to 80 km/s, which is over ten times the impact speeds from the anchor data. Due to these significant extrapolations, it has been deemed important to try to find better tools for extrapolating from existing data than empirical models. To this end, numerical simulations are being performed of impacts into a variety of Whipple shield configurations to determine the threshold of detached spall and hole size in rear walls of double-wall Whipple shields at conditions representative of meteoroid impacts. From these simulations, ballistic-limit models as a function of shield type, projectile material and size, impact speed and obliquity, have been developed for empirical model evaluation and refinement. This work discusses the aspects of simulation model verification, simulated conditions, and empirical model evaluation.

Keywords: MEM3, Whipple Shield, ballistic-limit equation

NOMENCLATURE

D	diameter (cm)
ϵ	strain
K	bulk modulus (GPa)
$\overline{m}$	areal density (g/cm^2)
$\overline{M}$	shield mass ratio
S	separation (cm)
t	thickness (cm)
T	temperature (eV)
U	ultimate tensile strength (MPa)
V	velocity (km/s)
$\bar{V}$	transition velocity (km/s)
Y	yield surface (MPa)
θ	obliquity $(°)$

Subscripts

B	bumper
c	critical
i	impact
j	counter
k	non-optimum exponent
l	optimum exponent
M	multi-layer insulation (MLI)
N	normal
o	initial
oo	tabular reference
p	projectile
R	rear wall
T	tube

1 INTRODUCTION

As NASA's human space flight focus shifts towards the Artemis mission and its architecture and away from the International Space Station’s low Earth orbit environment, there has been an increased emphasis on understanding and mitigating the risks posed by meteoroid impacts while balancing the mass of the station delivered to lunar orbit. For decades, the primary concern for spacecraft in low-Earth orbit has been the threat of collisions with orbital debris. However, as we venture further from Earth and establish a presence on the Moon and beyond, the threat of meteoroid impacts becomes a more significant contributing risk to crew safety. As a result, NASA is dedicating more resources to improved modeling of the meteoroid engineering model (MEM) [1], as well as, developing technologies to better assess the risk to Artemis structures.

The MEM revisions have necessitated the revisit of the performance of the Whipple shield with respect to meteoroids.

---

* Corresponding author: joshua.e.miller@nasa.gov

While MEM has long accounted for the high relative speeds of meteoroids, the updated version of MEM recognizes that many meteoroids that travel close to the Sun have had their volatile components ablated off leaving their higher density cores. This has been captured in the third iteration of MEM as a bimodal distribution on density, which is qualitatively shown in Fig. 1a [2]. Currently, MEM does not specify any other meteoroid properties than density. These two modes are centered at 0.857 g/cm^3 for the low-density population and 3.792 g/cm^3 for the high-density distribution. NASA programs have selected nylon at 1.15 g/cm^3 and alumina (Al_2O_3) at 3.895 g/cm^3, as shown in Fig. 1a, to represent these two populations for testing and analysis efforts.

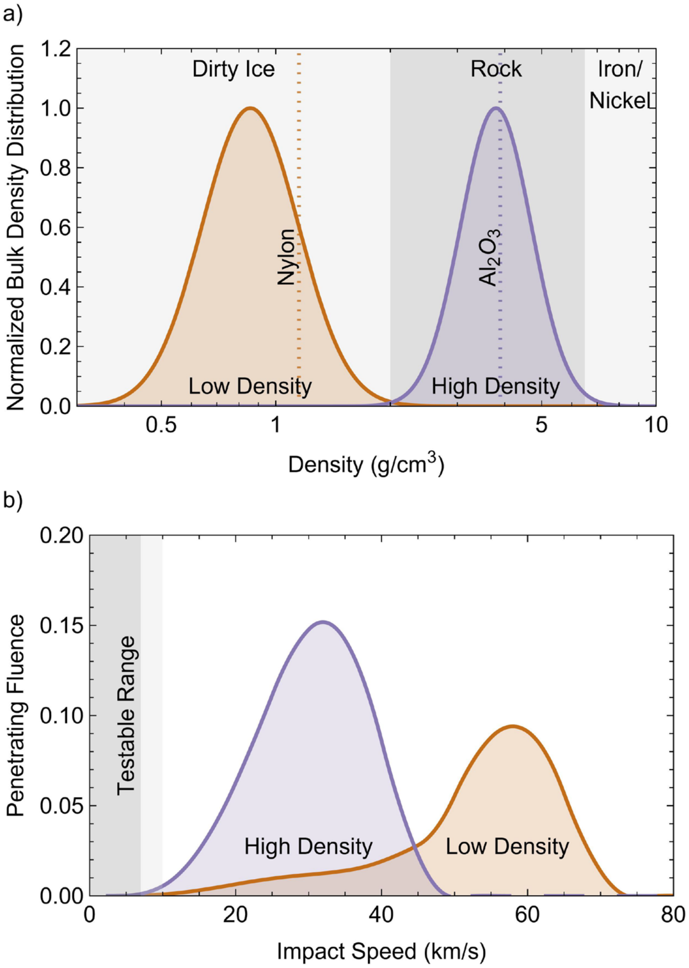

FIGURE 1: Meteoroid engineering model a) bulk density distribution and b) fluence speed dependence.

The relative speed of penetration fluence for a vehicle in a Near-Rectilinear Halo Orbit (NRHO) of the Moon is shown in Fig. 1b. The orbit goes from 3,000 km above the Moon at perilune to approximately 70,000 km above the Moon at apolune and has an orbital period of 7 days. Relative to the Sun, and therefore the meteoroid population, this orbit is largely equivalent to any other structure at 1 AU. As can be seen in Fig. 1b, the relative impact speed of penetration that is expected at Gateway from the high-density population is between 20 to 40 km/s, and for the low-density population it extends from 20 km/s to about 70 km/s with the bulk of the environment at 55 km/s.

As is also illustrated in Fig. 1b, these meteoroid populations are well above the impact speeds attainable by light-gas-guns which are limited to around 10 km/s. Because of this gap in capability, NASA Hypervelocity Impact Technology (HVIT) group is using numerical simulations grounded by model verification to develop shield performance models for addressing the meteoroid population defined by MEM3. This paper discusses the shield types being studied against the MEM3 environmental definition, as well as the numerical model development and verification for use at high speeds. This verified model is then used to study the effects of varying shield parameters and impact conditions for ballistic-limit model development.

2 MATERIALS AND METHODS

Among the shields used to protect from solid particle environments like meteoroids, the most ubiquitous are variants of the shield proposed by Fred Whipple in 1947 that now carries his name [3] and modeling quantified over the years by many authors [4-6]. The shield, in its simplicity, has proven to be a mass-efficient way of raising the size of the acceptable threat for reliability and survivability in the meteoroid environment. As an example of its widespread use, over 40% of the Gateway Space Station and its visiting vehicles, Fig. 2, can be classified as a variant of this shield, where the thickness of the bumper and the rear wall are t_B and t_R and S and $\overline{m_M}$ are the separation and areal density of the multi-layer insulation (MLI), respectively.

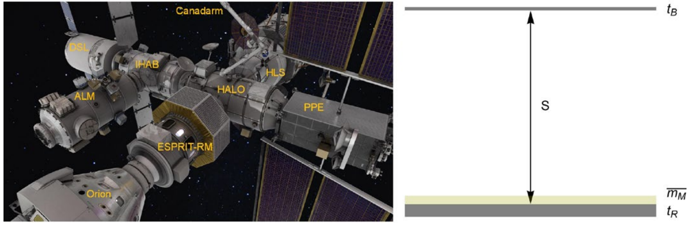

FIGURE 2: The Artemis Gateway architecture is a large space station that orbits the moon and relies heavily on variations of the Whipple shield to maintain integrity in the meteoroid environment.

Both the aluminum bumper and rear wall in this work use the tabular SESAME 3700 model for bulk thermodynamic properties that are energy and pressure scaled to their mean alloy molecular weight ($SR = \rho_{oo}/\rho_o$). The SESAME 3700 model includes melting and vaporization as well as ionization equilibrium models at low densities. The material is set to yield with a work hardening, strain-rate hardening, and thermal softening dependence based upon a Johnson-Cook formulation given in Fig. 3.

When the rear wall is taken as stainless steel, the tabular SESAME 2150 model for iron for bulk thermodynamic properties. Once again, the alloy is scaled to the mean molecular weight. The SESAME 2150 model includes four solid phases (alpha, gamma, epsilon, delta), melting, and vaporization.

The multi-layer insulation (MLI) is modeled using the Analytic EOS (ANEOS) 7310 for polyimide. The 7310 model is a solid-gas (sublimation) model with ionization; 7310 does not include a melting transition. The polyimide is assumed to have some linearity up to a thermally dependent yield surface. While MLI is made up of many very thin layers of materials like polyimide, in this work, the mass of MLI is split up between a pair of polyimide layers to preserve blanket mass while using solid density material.

Al6061 Bumper Constitutive Properties

Al SESAME 3700 EOS

ρ_{oo}=2.7g/cm^3, SR=0.999, ρ_o=2.703g/cm^3

Johnson-Cook yield surface

$$Y=(266.8+126.8\ \epsilon^{0.258})(1+0.015\ \mathrm{Ln}[\dot{\epsilon}])\left(1-\left(\frac{T-0.025\ \mathrm{eV}}{0.069\ \mathrm{eV}-0.025\ \mathrm{eV}}\right)\right)\mathrm{MPa}$$

U=361MPa, v=0.33

MLI Constitutive Properties

Polyimide ANEOS 7310

ρ_o=1.41g/cm^3, K=9.8GPa

Thermal dependent yield surface

$$Y=69.9\left(1-\left(\frac{T-0.025\ \mathrm{eV}}{0.042\ \mathrm{eV}-0.025\ \mathrm{eV}}\right)\right)\mathrm{MPa},\ U=69.9\mathrm{MPa},\ v=0.45$$

Al2219 Rear Wall Constitutive Properties

Al SESAME 3700 EOS

ρ_{oo}=2.7g/cm^3, SR=0.961, ρ_o=2.81g/cm^3

Johnson-Cook yield surface

$$Y=(274.9+432.8\ \epsilon^{0.258})(1+0.015\ \mathrm{Ln}[\dot{\epsilon}])\left(1-\left(\frac{T-0.025\ \mathrm{eV}}{0.069\ \mathrm{eV}-0.025\ \mathrm{eV}}\right)\right)\mathrm{MPa}$$

U=517MPa, v=0.33

CRES316L Rear Wall Constitutive Properties

Fe SESAME 2150 EOS

ρ_{oo}=7.87g/cm^3, SR=0.999, ρ_o=7.88g/cm^3

Johnson-Cook yield surface

$$Y=(606.3+1{,}1501\ \epsilon^{0.2507})(1+0.014\ \mathrm{Ln}[\dot{\epsilon}])\left(1-\left(\frac{T-0.025\ \mathrm{eV}}{0.157\ \mathrm{eV}-0.025\ \mathrm{eV}}\right)\right)\mathrm{MPa}$$

U=1,275MPa, v=0.283

High-Density Meteoroid Surrogate Constitutive Properties

Al_2O_3 SESAME B601 EOS

ρ_{oo}=3.969g/cm^3, ρ_p=3.895g/cm^3, P_s=100 MPa

Thermal dependent yield surface

$$Y=2.6\left(1-\left(\frac{T-0.025\ \mathrm{eV}}{0.173\ \mathrm{eV}-0.025\ \mathrm{eV}}\right)\right)\mathrm{GPa},\ U=260\mathrm{MPa},\ v=0.22$$

Low-Density Meteoroid Surrogate Constitutive Properties

Nylon ANEOS 7300

ρ_{oo}=1.15g/cm^3, K=5.3GPa

Thermal dependent yield surface

$$Y=62.4\left(1-\left(\frac{T-0.025\ \mathrm{eV}}{0.042\ \mathrm{eV}-0.025\ \mathrm{eV}}\right)\right)\mathrm{MPa},\ U=63\mathrm{MPa},\ v=0.4$$

FIGURE 3: Materials and material models used in shielding analysis.

The low-density meteoroid surrogate is modeled using the ANEOS 7300 for nylon. The 7300 model is also a solid-gas (sublimation) model with ionization, and a similar thermally dependent yield surface is used. It is noted at meteoroid impact speeds, the meteoroid will certainly be very far above yield, and accounting for elastic compression is only of practical importance to model verification.

The high-density meteoroid surrogate uses a SESAME B601 Al_2O_3 model developed for NASA and the Applied Physics Laboratory at Johns Hopkins University [7]. This model accounts for melting under shock loading at around 400 GPa and a complete dissociation starting at around 800 GPa with ionization in the reaction products: aluminum and monatomic oxygen. As with the low-density meteoroid, the relatively simple thermally dependent yield criterion is used for the surrogate.

These materials are set up in a three-dimensional solution space using the Sandia National Laboratory non-linear, structural-dynamics code, CTH [8]. The solution space is discretized with a constant cell size of 0.25 mm along the velocity vector of the projectile. Orthogonal to the projectile velocity vector the cell size is 0.25 mm out to 2.4 cm from the impact point and then increases linearly to 0.75 mm for an additional 4.8 cm; therefore, near the projectile flight path where most of the impact debris exists, the cells are 0.25 mm cubes. For normal impacts (i.e. the projectile velocity runs straight down the center of the shield), the negative values of x are just a reflection of the positive values and a reflection boundary condition is used at x=0 to reduce the size of the solution space. For all impacts, a reflection boundary condition is used at y=0 to minimize the solution space.

As meteoroid impact speeds imply that a significant quantity of gaseous plasma is going to be produced upon release from the high-pressure state, an ideal helium gas of 1 Pa at 4 K is used to fill the solution space to provide a small backfill to the impact debris. This backfill is necessary to keep the wave motion finite under the simplifications of CTH numerical techniques, but as it is a very low mass of backfill, there is a negligible effect on the simulation results. To maintain the backfill, all other boundary conditions are continuous pressure across the boundary with mass flow allowed out of the mesh.

2.1 Normal impact shield comparison

A small number of impact tests have been performed using smaller shields sized on a 0.17-caliber, two-stage, light-gas-gun at the NASA Remote Hypervelocity Test Laboratory in Las Cruces, NM to verify the numerical simulation model. The shield used for a Al_2O_3 meteoroid surrogate consisted of a 0.3 mm Al6061 bumper and a 1.0 mm Al2219 rear wall with a separation of 4.5 cm. The test used a 2.52 mm diameter Al_2O_3 projectile with a mass of 0.03267 g and impacted the target at 6.62 km/s normal to the target surface. This test produced a perforation of the rear wall with a mean diameter of 13.85 mm and a hole area of 124.8 mm^2.

A similar test was performed with a nylon projectile. The shield used for the nylon meteoroid surrogate consisted of a 0.3 mm Al6061 bumper and a 1.0 mm Al2219 rear wall with a separation of 1.5 cm. The test used a 2.75 mm diameter nylon projectile with a mass of 0.01243 g and impacted the target at 6.49 km/s normal to the target surface. The test produced a perforation of the rear wall with a mean diameter of 7.05 mm and a hole area of 19.4 mm^2.

2.2 Debris Cloud

The evolution of the debris cloud while it traversed the expansion gap of the Whipple shield was captured by a Shimadzu HyperVision HPV-X camera at one million frames per second. For the high-density meteoroid surrogate, a sequence of nine grayscale images from the camera are shown in Fig. 4 from just prior to impact of the Al_2O_3 projectile at 1 μs intervals. Overlain on the camera images are density contours from the CTH simulation of the test. The simulation shows compressed densities up to 10 g/cm^3 and released material down to 10^{-4} g/cm^3.

The images progress in time from left to right and from top to bottom. The highest mass concentration, along with the highest density fragments, are in the center of the debris cloud. Advancing in front of the main projectile debris is the shock wave released aluminum bumper, which releases to very low densities that are near the detection threshold of the Shimadzu cameras. The bulk of the projectile material remains at high densities, and this material results in the bulk of the damage to the rear wall. As can be seen, the simulation tracks the expanding debris well for the main components of debris.

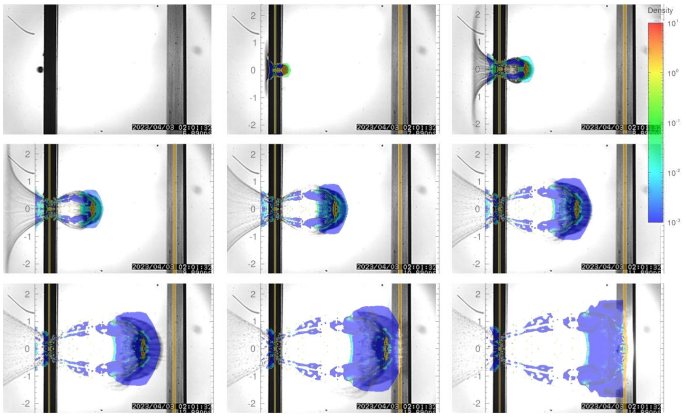

FIGURE 4: Debris cloud evolution for the high-density meteoroid surrogate impact test with simulation results overlain. Frames are at 1 μs interval moving left to right, top to bottom.

For the low-density meteoroid surrogate, a similar sequence of nine grayscale images from the camera are shown in Fig. 5. As the separation between the two walls is only 1.5 cm, the impact remnants traverse the shield in a limited number of frames. Once again, density contours from the CTH simulation are shown over the top of the still images from the video at the same time interval. Here too, the simulations are shown as density contours from 10 g/cm^3 to 10^{-4} g/cm^3. It can be seen that the, projectile and bumper materials, both release to less than 1 g/cm^3. Both the speed of the debris cloud and extent of the debris cloud expansion are well modeled by the simulation.

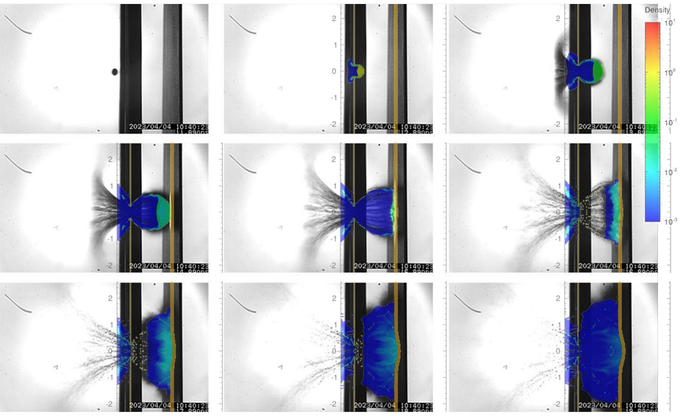

FIGURE 5: Debris cloud evolution for the low-density meteoroid surrogate impact test with simulation results overlain. Frames are at 1 μs interval moving left to right, top to bottom.

2.3 Rear Wall Comparison

The final comparison to the benchmark cases is from the recovered rear walls. The Al_2O_3 rear wall comparison is in Fig. 6. In this figure the damage of the experimental rear wall (left) is compared to the mask of the simulated rear wall damage (right). As can be seen in the experiment, the central crater completely eroded through the rear wall and the ring craters merged with the central crater. This is compared to the simulated wall where the central crater also eroded through the rear wall, but the ring craters did not completely merge with the central crater. The overall damage dimensions of the eroded hole in the rear wall includes a maximum damage width of 19.6 mm and mean diameter of 13.85 mm; whereas, the simulation has a maximum damage width of 17.6 mm and mean diameter of 12.5 mm. As can be seen in Fig. 6 the through-hole area is also well calculated with the simulated area being within 2% of the observed value.

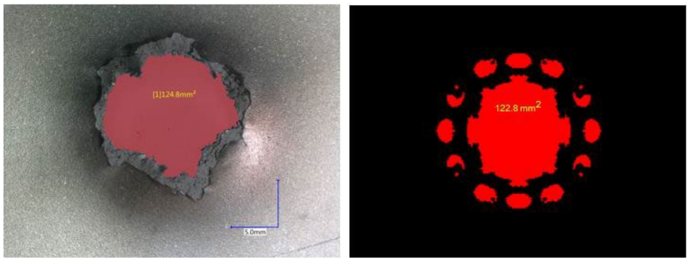

FIGURE 6: Comparative recovered rear wall damage image to the simulated damage to the rear wall for the high-density meteoroid surrogate.

The nylon rear wall comparison is in Fig. 7. In this figure a direct comparison of the damage to the experimental rear wall (left) is shown next to the mask of the simulated rear wall damage (right). As can be seen in the experiment, the failure is a tensile tearing of the rear wall. This is compared to the simulated wall where the prediction is also a tensile tearing of the rear wall. The overall damage dimensions of the hole in rear wall include a maximum damage width of 13.9 mm and mean diameter of 5.0

mm; whereas, the simulation has a maximum damage width of 13.1 mm and mean diameter of 4.5 mm. As can be seen in Fig. 7 the through-hole area is also well calculated with the simulated area.

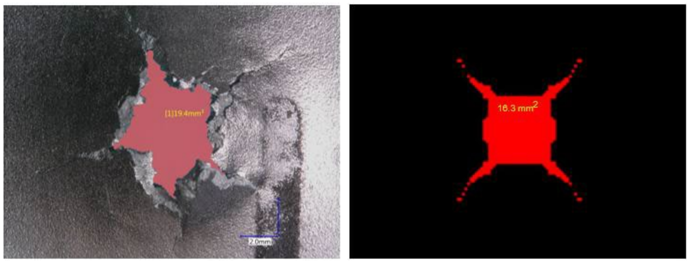

FIGURE 7: Comparative recovered rear wall damage image to the simulated damage to the rear wall for the low-density meteoroid surrogate.

3 RESULTS AND DISCUSSION

Having developed a suitable numerical model, the model has been exercised through an extensive number of simulations to develop a ballistic-limit model for the critical diameter, D_c, for Whipple shields:

$$\begin{aligned} V_N \le \left.\begin{matrix}1.\\3.\end{matrix}\right|_0 \qquad & D_0 = 0.925\,\frac{\frac{\overline{m_B}}{2.7}+1.035\,\bar{M}\;\overline{m_R}\,\rho_R^{\frac{1}{5}}}{\rho_p^{\frac{1}{2}}\,V_i^{\frac{2}{3}}\,Cos^{\frac{5}{3}}[\theta_i]} \\ \left.\begin{matrix}2.\\7.5.\end{matrix}\right|_1 \le V_N \le \left.\begin{matrix}3.\\9.5\end{matrix}\right|_2 \qquad & D_1 = 0.873\,\frac{\bar{M}\;\overline{m_R}^{\frac{2}{3}}\,S^{\frac{1}{3}}\,\rho_R^{\frac{2}{9}}}{\rho_B^{\frac{1}{9}}\;\rho_p^{\frac{1}{3}}\,V_i^{\frac{2}{3}}\,Cos^{\frac{2}{3}}[\theta_i]} \\ V_N \ge \left.\begin{matrix}10.\\31.5\end{matrix}\right|_3 \qquad & D_2 = 0.526\,\frac{\bar{M}\,\overline{m_R}^{\frac{2}{3}}\,S^{\frac{1}{2}}\,\rho_B^{\frac{1}{3}}\,\rho_R^{\frac{1}{9}}}{\rho_p^{\frac{1}{2}}\,V_i^{\frac{1}{3}}\,Cos^{\frac{3}{4}}[\theta_i]} \end{aligned} \qquad (1)$$

where V_N is the normal component of impact velocity vector to the shield, $V_N = V_i\,Cos[\theta_i]$, and the transition regimes $D_{\frac{1}{2}}$ and $D_{\frac{3}{2}}$ are given by:

$$D_{\frac{2\,j+1}{2}} = \frac{\left(D_{j+1}[\bar{V}_{2\,j+1}]-D_j[\bar{V}_{2\,j}]\right)}{\left(\bar{V}_{2\,j+1}-\bar{V}_{2\,j}\right)}\left(V_N-\bar{V}_{2\,j}\right)+D_j\left[\bar{V}_{2\,j}\right] \qquad (2)$$

where $\bar{V}$ are four pairs of transition speeds with the top being for low-density meteoroids and the bottom being high-density meteoroids. The transition velocities are: $\bar{V}_0$ is $1.\,km/s$ or $3.\,km/s$, $\bar{V}_1$ is $2.\,km/s$ or $7.5\;km/s$, $\bar{V}_2$ is $3.\,km/s$ or $9.5\;km/s$ and $\bar{V}_3$ is $10.\,km/s$ is $31.5\;km/s$, where the first value is for low-density meteoroids and the second is for high-density meteoroids.

The critical diameter, D_c, is the piecewise function of D_j. When V_N is less than the first velocity transition (V_N less than 1 km/s and 3 km/s for low-density and high-density meteoroid, respectively), then $j=0$ and $D_c = D_0$. This regime is the traditionally observed ballistic regime, albeit, affected by the new classes of materials chosen as meteoroid. Between this first and the next velocity regime (V_N less than 2 km/s and 7.5 km/s for the low-density and high-density meteoroid, respectively), $j=0$ and $D_c = D_{1/2}$, which is a linear interpolation representing the partial fragmentation of the impact remnants. Above $\bar{V}_1$ is a fragmented solid or a molten mass that can expand over a larger area of the rear wall, and the critical diameter is represented by $j=1$ and $D_c = D_1$ until the next velocity transition (V_N less than 3 km/s and 9.5 km/s for low-density and high-density meteoroid, respectively). This third velocity transition, $j=1$ and $D_c = D_{3/2}$, is descriptive of the onset of sublimation of the impact remnants and will be shown to be complete by the final velocity transition ($\bar{V}_3$ equal 10 km/s and 31.5 km/s for low-density and high-density meteoroid, respectively). Above this final transition, $j=2$ and $D_c = D_2$, the initial impact remnants have been found to be a completely disassembled plasma that is free to expand prior to impacting the rear wall.

The other terms in the D_j equations are $\overline{m_B}$ and $\overline{m_R}$, which are the areal density (product of thickness and density) of the bumper and rear wall, respectively. If multi-layer insulation is present on the rear wall, this mass has been added to the rear wall: $\overline{m_R} = t_R\,\rho_R + \overline{m_M}$. The densities of the impact materials, ρ_p, ρ_B, and ρ_R are for the projectile, bumper and rear wall, respectively. S is the separation between the bumper and the rear wall. The final term, $\bar{M}$, is a mass ratio term for the shield walls given by:

$$\begin{aligned} \frac{\overline{m_B}}{\overline{m_R}} \le \frac{1}{2} \quad & \bar{M} = \left(\frac{4}{5}\,\frac{\overline{m_B}+\overline{m_R}}{\overline{m_R}}\right)^k \\ \frac{\overline{m_B}}{\overline{m_R}} > \frac{1}{2} \quad & \bar{M} = \left(\frac{6}{5}\right)^k\left(2\,\frac{\overline{m_B}}{\overline{m_R}}\right)^l \end{aligned} \qquad (3)$$

where k and l are regime dependent with $k = 2/3$ and $l = 1/2$ for $j=0$ and $j=1$ (low- and mid-velocity regimes), and $k = 5/2$ and $l = 1/3$ for $j=2$ (high-velocity regime).

Together Eqn. 1, 2 and 3 along with the definitions provide a complete model for the critical diameter as a function of impact parameters related to the shield and the environment. In all cases, the coefficients are tied to the use of cgs units except for speeds that use km/s. A comparison of this model with the accumulated data are shown in the following subsections.

3.1 Normal impact with wall separation dependence

The normal impact of high-density particles has been studied for three different wall separations: 2.4, 14 and 19 cm. The thicknesses of the Al6061 bumper and Al2219 rear wall are held constant at 0.8 mm and 3.0 mm, respectively. A representative composite image from two different impact simulations is shown in Fig. 8. The left image of Fig. 8 is of a 4.0 mm Al_2O_3 particle that hit at 40 km/s, and the right image is a 4.4 mm Al_2O_3 particle at the same speed. The images are density contours stacked on top of each other showing the initial impact condition at 0 μs, the debris cloud at 1.5 μs and 3.0 μs and the profile of the rear wall 30 μs after the initial impact at the bottom. As can be seen in the side-by-side images, the larger particle produces a higher density debris cloud at the same point in time post initial impact, and as a result the rear wall has an attached spall bubble for the 4.0 mm Al_2O_3 and detached spall for the 4.4 mm Al_2O_3 particle. This transition between attached and detached spall is the desired ballistic-limit for failure of the rear wall.

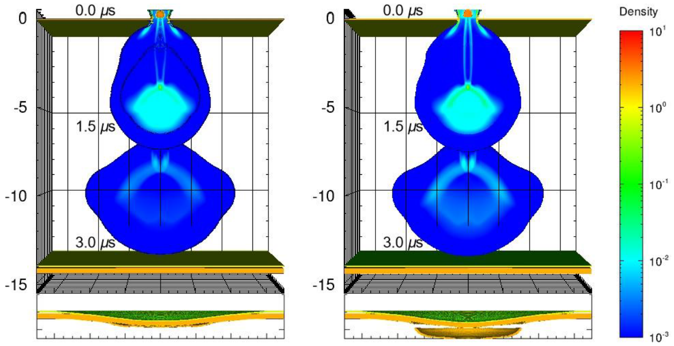

FIGURE 8: Side by side comparison of high-density meteoroid impact at 40 km/s just below the critical diameter (left) and just above (right). Snap shots of the debris cloud are shown at 1.5 μs interval, and an image of the final state of the rear wall is shown at the bottom.

The pairing in Fig. 8 is just one impact condition, but it takes a much broader look above the testable range (max about 7 to 10 km/s) to check out a ballistic limit model like that from this section. The collection of sixty-nine impact simulations with the model of this section is shown in Fig. 9. The three separations that have been looked at are color matched to the model, with the final state of the rear wall shown by shading: open circle (rear wall intact), light-shaded circle (detached spall) and dark-shaded circle (perforation). For the purposes of this modeling, detached spall and perforation are counted as a failure. As can be seen, the model represents the obtained simulation data well.

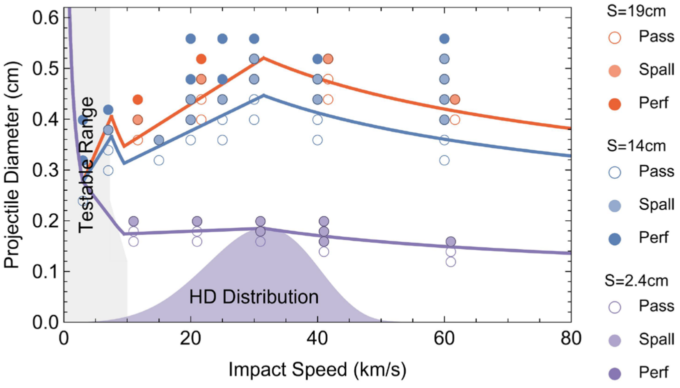

FIGURE 9: Collection of the normal impact, high-density meteoroid surrogate data with varying separation between the shield, and all other shield aspects held constant. Curves correspond to the model of this section with the shield and impact conditions as inputs.

Similarly, the composite image of two different impact simulations for a low-density meteoroid surrogate are shown in Fig. 10. The left image of Fig. 10 is of a 7.0 mm nylon particle that hit at 60 km/s, and the right image is an 8.0 mm nylon particle at the same speed. The images show the initial impact condition at 0 μs, the debris cloud at 1.0 μs and 2.0 μs and the profile of the rear wall 30 μs after the initial impact at the bottom. As it is with the high-density meteoroid surrogate, the larger particle produces a higher density debris cloud at the same point in time post initial impact. The 7.0 mm particle produced a spall bubble, and the 8.0 mm particle produced detached spall.

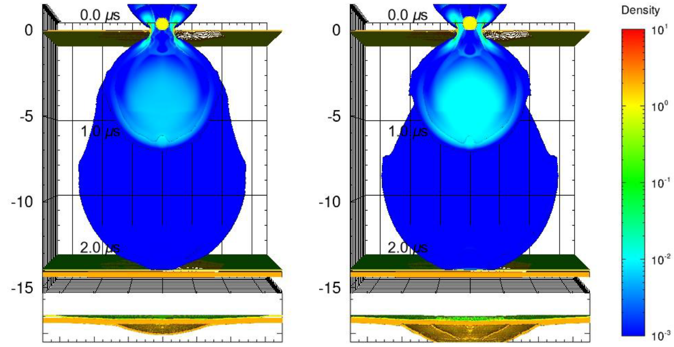

FIGURE 10: Side by side comparison of low-density meteoroid impact at 60 km/s just below the critical diameter (left) and just above (right). Snap shots of the debris cloud are shown at 1.0 μs interval, and an image of the final state of the rear wall is shown at the bottom.

The collection of forty-three impact simulations is shown in Fig. 11. The two separations that have been looked at are color matched to the model, with the final state of the rear wall shown by shading: open circle (rear wall intact), light-shaded circle (detached spall) and dark-shaded circle (perforation). As with the high-density particles, the model represents the obtained simulation data well.

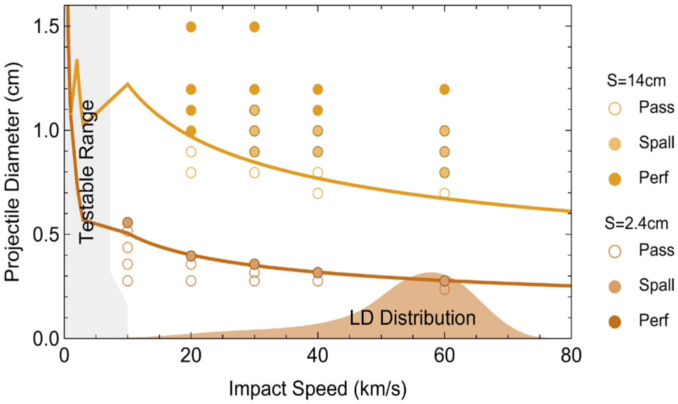

FIGURE 11: Collection of the normal impact, low-density meteoroid surrogate data with varying separation between the shield, and all other shield aspects held constant. Curves correspond to the model of this section with the shield and impact conditions as inputs.

Low-density meteoroid surrogates have been considered in all the additional scenarios from the following sub-sections, for brevity in this work, the remainder of the discussion focuses on the higher risk, high-density meteoroid surrogates.

3.2 Oblique impact dependence

The oblique impact of high-density particles has been studied for 14 cm separations at 0°, 30° and 45°. The thicknesses of the Al6061 bumper and Al2219 rear wall are held constant at 0.8 mm and 3.0 mm, respectively. For oblique impacts, the velocity vector of the projectile continues down the axis with the constant cubic 0.25 mm mesh just like the 0° to normal impacts. The plates are rotated about an orthogonal axis to achieve the desired obliquities.

A representative image of two different impact simulations for oblique impacts is shown in Fig. 12 at 50 μs after initial impact. The left and right images of Fig. 12 are of a 4.8 mm and 5.2 mm Al_2O_3 particle that hit 45° to normal at 40 km/s, respectively. The smaller 4.8 mm particle dented the rear but did not result in a perforate or induce spall, so the 4.8 mm particle did not fail the shield. The larger 5.2 mm particle produces a hole in the rear wall of the shield, and this simulation is counted a failure of the shield.

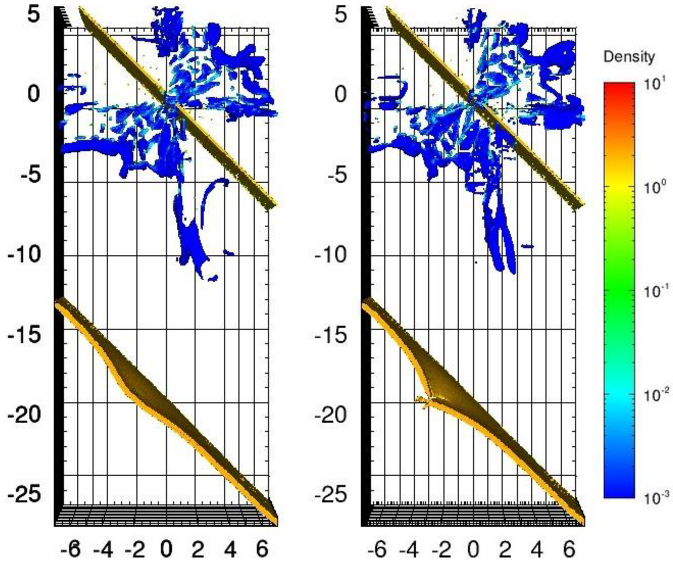

FIGURE 12: Side by side comparison of the final state of the rear wall for high-density, oblique meteoroid impacts at 40 km/s just below the critical diameter (left) at 4.8 mm and just above (right) at 5.2 mm.

Many additional oblique simulations have been performed in developing the ballistic-limit model given here. In Fig. 13, sixty impact simulations are shown. As has been done before, the final state of the rear wall is shown by shading: open circle (rear wall intact), light-shaded circle (detached spall) and dark-shaded circle (perforation). The different obliquities are colored navy for normal impact, orange for 30° to normal impact and green for 45° to normal impact.

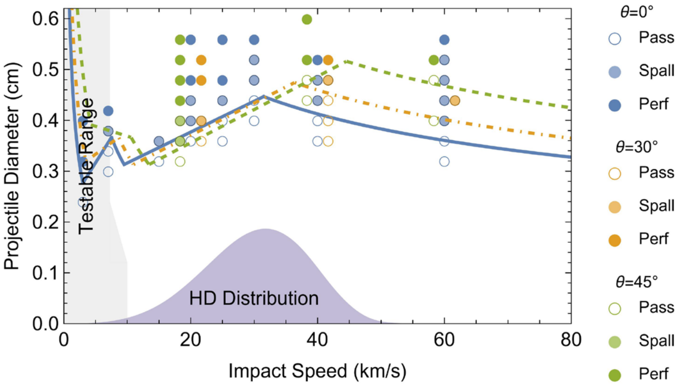

FIGURE 13: Collection of the oblique impact, high-density meteoroid surrogate data. All shield aspects are held constant, and the impact obliquity and speed are varied. The different obliquities are shown solid for normal impact, dot-dashed for 30° to normal impact and dashed for 45° to normal impact.

Overplotted on the simulated data points is the color matched model reported herein, with the 30° to normal curve dot-dashed and the 45° to normal curve dashed to further help distinguish the obliquities. As can be seen, the model reproduces the obliquity dependence of the simulations well.

3.3 Comparison of non-aluminum rear walls

The normal impact of high-density particles into a shield with a 2.4 cm separation and a 0.8 mm thick Al6061 bumper has been performed for both a 3.0 mm thick Al2219 rear wall and a 1.1 mm thick CRES316L stainless steel rear wall, which both have an areal density of about $0.85\ g/cm^2$. The collection of twenty-eight impact simulations is shown in Fig. 14, with the final state of the rear wall shown by shading: open circle (rear wall intact), light-shaded circle (detached spall) and dark-shaded circle (perforation). To separate the different simulation points, Al rear walls are shown in purple, and SS rear walls are shown in magenta.

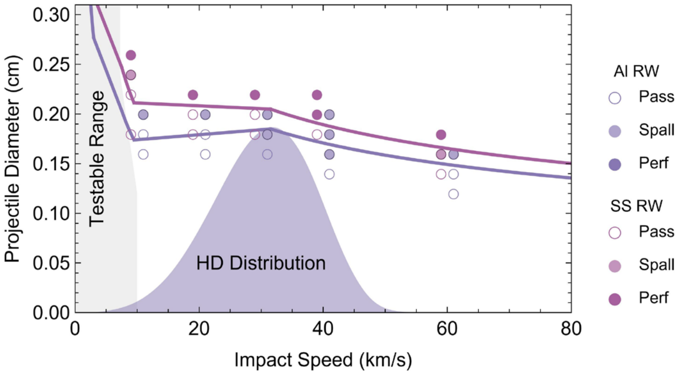

FIGURE 14: Collection of the normal impact, high-density meteoroid surrogate data. Shield rear wall material is varied but mass per unit area is held constant. All other shield aspects are held constant. Curves correspond to the model of this section with the shield and impact conditions as inputs.

Overplot with the data is the performance model from this work. Although, the rear wall mass is the same for the two types of rear wall material, the rear wall performance is higher for the SS rear wall than the Al rear wall. This behavior has been captured in the model as demonstrated by the curves in Fig. 14.

3.4 Comparison of non-standard wall ratios

The final look is for rear wall performance when non-standard shield size ratios are used. Commonly shields have a rear wall mass to bumper mass ratio of around 3 to 4. In this look the separation is held at 9.6 cm and the bumper thickness is held at 0.8 mm of Al6061, but the rear wall thickness is varied from 1.5 mm, 6 mm and 9 mm, which represents mass ratios of about 2, 8 and 12, respectively. These shield configurations have been studied with high-density particles impacting into the shield.

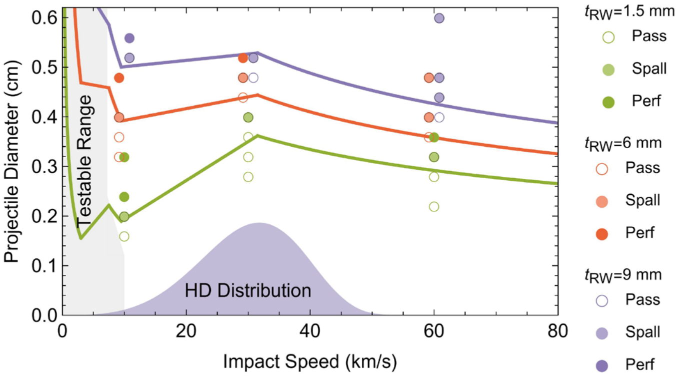

FIGURE 15: Collection of the normal impact, high-density meteoroid surrogate data. Shield rear wall thickness is significantly varied. All other shield aspects are held constant. Curves correspond to the model of this section with the shield and impact conditions as inputs.

The collection of thirty impact simulations is shown in Fig. 15, with the final state of the tube wall shown by shading: open circle (rear wall intact), light-shaded circle (detached spall) and dark-shaded circle (perforation). Overplot with the data is the performance model from this work. As can be seen, the impact of lowering the mass of the rear wall is a significant performance hit for low speeds, but for higher speed meteoroids, the impact is reduced. This behavior has been captured in the model as demonstrated by the curves in Fig. 15 that are color matched to the simulation condition.

4 CONCLUSION

This paper has documented the recent efforts by NASA HVIT group to develop broad-ranging ballistic-limit models of the meteoroid environment for use in early phase design development of Artemis architecture. As current meteoroid environments have the relative impact speed of meteoroid populations well above the impact speeds attainable by any light-gas-gun, a gap in capability for ballistic-limit modeling is evident. To make progress towards these generalized design equations, NASA HVIT is using numerical simulations grounded by model verification to develop shield performance models for addressing the meteoroid population defined by MEM3. This paper has documented the results of this simulation and verification effort, as well as the resultant design ballistic-limit equations. While many simulations have been performed and addressed in the modeling, these equations should still be considered preliminary and verified with actual shield parameters as the design matures. As such continued effort will be made to model new regions of Artemis architecture and corresponding updates to the generalized model will be made.

ACKNOWLEDGEMENTS

The author wishes to gratefully acknowledge the Jacobs JETS-II contract 80JSC022DA035 in its support to the NASA Johnson Space Center Hypervelocity Impact Technology group and sponsorship to University of Texas at El Paso under J2N30009TMS. The United States Government retains, and by accepting the article for publication, the publisher acknowledges that the United States Government retains, a non-exclusive, paid-up, irrevocable, worldwide license to publish or reproduce the published form of this work, or allow others to do so, for United States Government purposes.

REFERENCES

[1] Moorhead, A.V. NASA Meteoroid Engineering Model (MEM) Version 3, NASA/TM-20202205555, NASA Marshall Space Flight Center, Huntsville, Alabama, 2020.

[2] Moorhead, A.V., Kingery, A. Ehlert, S. NASA's Meteoroid Engineering Model (MEM) 3 and its ability to replicate spacecraft impact rates, J. of Spacecraft and Rockets, vol. 57, pp. 160-175, 2020.

[3] Whipple, F.L., Meteorites and space travel, Astronomical Journal, No. 1161, 132, 1947.

[4] Christiansen. E.L., et. al. Handbook for Designing MMOD Protection, NASA/JSC-64399, NASA Johnson Space Center, Houston, Texas, 2009.

[5] Schonberg, W.P., "Assessing the Predictive Capability of the NNO Ballistic Limit Equation for Low-Density Projectile Impact", ASCE Journal of Aerospace Engineering, Vol. 36, No. 1, 2023, Article No. 04022119.

[6] Schonberg, W.P., "Improved Ballistic Limit Equations for High-Speed Non-Aluminum Projectiles Impacting Aluminum Dual-Wall Spacecraft Systems", Springer Nature Applied Sciences Journal, Vol. 2, No. 8, 2020, Article No. 1426-2020.

[7] Kerley, G. I. "Equation of State and Constitutive Models for Numerical Simulations of Dust Impact on the Solar Probe", Kerley Technical Services, Report on Contract 949182, Appomattox, VA 2009.

[8] Duncan, G.C. and Key, C.T. FY21 Improvements to the New CTH Code Verification & Validation Test Suite, SAND2022-7834, Albuquerque, New Mexico, 2022.